Nonlinear Combustion Instability in a Multi-Injector Rocket Engine

Juntao Xiong,[*] Hugh Morgan,[†] Jeremy Krieg,[†] Feng Liu,[‡] and William A. Sirignano[‡]
University of California, Irvine, Irvine, California 92697

A computational study is presented of the nonlinear combustion instability of a multi-injector rocket engine. The study addresses a choked nozzle and a combustion chamber with 10 and 19 coaxial injector ports. Computations using a three-dimensional unsteady $k - \omega$ shear-stress transport delayed detached-eddy simulation method provide detailed time-resolved information about the combustion instability. The spontaneous longitudinal-mode instability is observed for the 10- and 19-injector geometries with a combustion-chamber diameter of 28 cm. The triggered tangential and longitudinal instability modes are obtained for the 19-injector geometry with a combustion-chamber diameter of 43 cm by pulsing the injector mass flux. It is shown that an oscillating combustion-chamber flow can be triggered to a new mode with a larger disturbance amplitude. The streamwise vorticity created by the instability impacts the heat release in a manner that supports the instability. A preliminary study of injector-size scaling effects is performed by comparison of the 10- and 19-injector combustors.

Nomenclature

$\bar{A}$	=	preexponential chemical rate constant, 1/s
c_p	=	specific heat at constant pressure, $J/(kg \cdot K)$
D_c	=	diameter of combustor chamber, cm
D_{fuel}	=	outer diameter of coaxial injector, cm
D_{kj}	=	mass diffusivity for species k in j direction, m^2/s
D_{ox}	=	inner diameter of coaxial injector, cm
D_t	=	diameter of nozzle throat, cm
E	=	stagnation internal energy, J
e	=	stagnation specific internal energy, J/kg
H	=	stagnation internal enthalpy, J
h	=	specific enthalpy, J/kg
h_s	=	stagnation specific enthalpy, J/kg
K	=	injector scaling coefficient, s^2/m
k	=	turbulent kinetic energy, m^2/s^2
$L_{chamber}$	=	length of combustion chamber; 50 cm
L_{throat}	=	distance between injector plate and choked nozzle; 33 cm
n	=	power of the velocity difference
p	=	static pressure, bar
q_i	=	energy flux in ith direction, $J/(m^2 \cdot s)$
R	=	mixture specific gas constant, $J(kg \cdot K)$
Rad	=	radius of the chamber, cm
R_{throat}	=	radius of the throat, cm
T	=	temperature, K
t	=	time, s
u_i	=	velocity components, m/s
$V_{k,i}$	=	correction velocity for species k in the ith direction, m/s
W	=	total molecular weight, kg/mol
W_k	=	molecular weight of species k, kg/mol
X_k	=	mole fraction of species k
x_i	=	position, m
Y_k	=	mass fraction of species k
γ	=	ratio of specific heats
ϵ	=	magnitude coefficient
η_{CH_4}	=	reaction efficiency
λ	=	total thermal diffusivity, m^2/s
λ_k	=	thermal diffusivity of species k, m^2/s
μ	=	total dynamic viscosity, $kg/(m \cdot s)$
μ_k	=	dynamic viscosity of species k, $g/(m \cdot s)$
μ_t	=	turbulent eddy viscosity, $g/(m \cdot s)$
ν_t	=	turbulent kinematic viscosity, $g/(m \cdot s)$
ρ	=	mass density, kg/m^3
τ_{ij}	=	shear stress tensor, Pa
ω	=	specific rate of dissipation
$\dot{\omega}_k$	=	reaction rate of species k, $kg/(m^3 \cdot s)$

*Associate Specialist, Department of Mechanical Aerospace Engineering. Member AIAA.

†Graduate Student, Department of Mechanical and Aerospace Engineering.

‡Professor, Department of Mechanical and Aerospace Engineering. Fellow AIAA.

I. Introduction

COUPLING mechanisms between acoustic waves and flames control two important phenomena in the development of modern combustion system: combustion dynamics and combustion instability [1]. Noise in the combustion process is directly related to vortex shedding. For the combustion instability, flames create noise but are also influenced by the noise leading to a resonant interaction. In general, the combustion instability is an undesired and harmful phenomenon. The resulting large-amplitude pressure oscillation can eventually damage the engine.

Combustion instability has been studied for many decades. An excellent compilation of works during the 1950s and 1960s was edited by Harrje and Reardon [2]. Also, a discussion of the F-1 rocket-motor instability problems was given by Oefelein and Yang [3]. During the period, most of the physics of the oscillation were identified. The longitudinal-mode linear instability was addressed extensively by Crocco and Cheng [4,5]. The two-parameter (n, n, τ) coupling between combustion and acoustics was developed for the stability analysis application. Sirignano and Crocco [6] and Mitchell et al. [7] performed nonlinear analyses for the longitudinal mode with shock-wave formation with spontaneous and triggered instabilities. Later, Zinn extended the theory for a transverse mode analysis [8]. Culick [9] noted two general types of acoustical combustion instability: driven instability and self-excited instability. Driven instability is more relevant in solid-propellant rocket engines. Self-excited instability is more relevant in liquid-propellant rocket engines. Self-excited instability includes linear and nonlinear instabilities. The linear instability indicates spontaneous instability. The nonlinear instability indicates triggered instability. A larger-than-threshold disturbance is required to trigger the instability. A detailed history of theoretical and experimental research was reviewed by Nguyen and Sirignano [10].

The combustion instability mechanism is very complex due to the nonlinear dynamics system involving the possible injector-to-injector interactions and interactions with the feed system and upstream manifold. Systematic experimental studies of combustion instability are very difficult because of the expense and the limitation of current measurement techniques [11,12]. With the recent rapid increase of computer power and new numerical algorithm development, numerical simulations are used to study the combustion instability of complex systems, which provides a more complete picture of the combustion instability mechanism than can be obtained from experimental data. There are several single-injector and multi-injector studies [10,13–15]. Oefelein and Yang [13] simulated two dimensional single-injector flow with 24 chemical reactions using a large-eddy simulation (LES). Nguyen et al. [14] and Nguyen and Sirignano [10] developed a highly efficient solver using the delayed detached-eddy simulation and compressible flamelet progress variable models with the assumption of infinitely fast chemical reaction. The flame dynamics occurred across three different instability regimes; fully unstable, semistable, and completely stable were examined. Also, the complex thermochemical mechanisms promoting combustion instability were analyzed. Urbano et al. [15] performed the LES for a hydrogen–oxygen liquid-rocket engine with 42 coaxial injectors. The simulation was performed for two operating conditions investigated experimentally at the DLR, German Aerospace Center laboratory. A pressure disturbance with a first transverse modal distribution was superimposed on the initial solution. They found that the oscillation is quickly dissipated when a small pressure disturbance is applied, whereas the oscillation reaches a limit cycle when a greater-than-threshold pressure disturbance is applied. A systematic numerical simulation of a multi-injector system remains to be demonstrated.

To better understand the effect of pressure disturbances on the stability of the reacting flow in a rocket-engine combustor with multiple injectors and a choked nozzle, a computational study is performed in this paper. Previous work in two dimensions [10,14,16–22] has shown the growth and decay of pressure oscillations. We attempt to understand the growth and decay of similar pressure disturbances in a three-dimensional geometry. The open-source computational fluid dynamics software OpenFOAM is used for this study. The study is conducted for a choked nozzle combustion chamber with 10 and 19 coaxial injector ports. We begin by describing the governing equations, the boundary conditions, and the chemistry models. To trigger the longitudinal- and tangential-mode instabilities, pulsing excitation of the injector mass flux is applied. Then, the simulation results are qualitatively analyzed. At the end, the injector-size scaling effects are discussed.

II.   Numerical Method

A.   Governing Equations

The compressible Navier–Stokes equations can be expressed as follows:

$$\frac{\partial \rho}{\partial t} + \frac{\partial (\rho u_j)}{\partial x_j} = 0 \tag{1}$$

$$\frac{(\partial \rho u_i)}{\partial t} + \frac{\partial (\rho u_i u_j)}{\partial x_j} = \frac{\partial \tau_{ij}}{\partial x_j} - \frac{\partial p}{\partial x_i} \tag{2}$$

$$\frac{\partial (\rho E)}{\partial t} + \frac{\partial ((\rho E + P) u_j)}{\partial x_j} = \dot{\omega}_T - \frac{\partial q_i}{\partial x_i} + \frac{\partial (\sigma_{ij} u_i)}{\partial x_j} \tag{3}$$

where the viscous stress tensor τ_{ij} is given by

$$\tau_{ij} = \tau_{ij}^L + \tau_{ij}^T \tag{4}$$

$$\tau_{ij}^L = \mu \left(\frac{\partial u_i}{\partial x_j} + \frac{\partial u_j}{\partial x_i} \right) - \frac{2}{3} \mu \frac{\partial u_k}{\partial x_k} \delta_{ij} \tag{5}$$

$$\sigma_{ij} = \tau_{ij} - p \delta_{ij} \tag{6}$$

Note that $\dot{\omega}_T$ represents the heat release rate due to combustion, and q_i represents the energy flux and is given by

$$q_i = -\lambda \frac{\partial T}{\partial x_i} + \rho \sum_{k=1}^{NS} h_k Y_k V_{k,i} \tag{7}$$

The first term in q_i represents Fourier's conduction law, and the second term represents energy transport via the diffusion of species with different specific enthalpies. $V_{k,i}$ represents the diffusion velocity and is defined as

$$V_{k,i} = -\frac{D_k}{X_k} \frac{\partial X_k}{\partial x_i} \tag{8}$$

The species transport equation is

$$\frac{\partial (\rho Y_k)}{\partial t} + \frac{\partial (\rho u_j Y_k)}{\partial x_j} = \frac{\partial}{\partial x_j} \left(\rho D_{kj} \frac{W_k}{W} \frac{\partial X_k}{\partial x_j} \right) + \dot{\omega}_k; = 1, \ldots, NS \tag{9}$$

where W_k is the species molecular weight, W is the total molecular weight, D_k is the coefficient of species diffusion, and $\dot{\omega}_k$ is the generation of species due to chemical reactions.

B.   Turbulence Model

The closure turbulence model used to evaluate the turbulent shear stress τ^T and viscosity μ_t is the $k - \omega$ shear-stress transport (SST)-based [23] detached-eddy simulation (DES) [24] turbulence model. The $k - \omega$ SST DES equations are

$$\frac{\partial (\rho k)}{\partial t} + \frac{\partial (\rho u_j k)}{\partial x_j} = P - \rho k^{3/2}/\tilde{l} + \frac{\partial}{\partial x_j} \left[(\mu + \sigma_k \mu_t) \frac{\partial k}{\partial x_j} \right] \tag{10}$$

$$\frac{\partial (\rho \omega)}{\partial t} + \frac{\partial (\rho u_j \omega)}{\partial x_j} = \frac{\gamma}{\nu_t} P - \beta \rho \omega^2 + \frac{\partial}{\partial x_j} \left[(\mu + \sigma_\omega \mu_t) \frac{\partial \omega}{\partial x_j} \right]$$
$$+ 2(1 - F_1) \frac{\rho \sigma_{\omega 2}}{\omega} \frac{\partial k}{\partial x_j} \frac{\partial \omega}{\partial x_j} \tag{11}$$

where

$$P = \tau_{ij} \frac{\partial u_i}{\partial x_j} \tag{12}$$

The turbulent eddy viscosity is given by

$$\mu_t = \frac{\rho a_1 k}{\max(a_1 \omega, \Omega F_2)} \tag{13}$$

The turbulent shear stress is calculated using

$$\tau_{ij}^T = 2 \mu_t \left(S_{ij} - \frac{1}{3} \frac{\partial u_k}{\partial x_k} \delta_{ij} \right) - \frac{2}{3} \rho \kappa \delta_{ij} \tag{14}$$

F_1 and F_2 represent blending functions. The model constants β^*, σ_k, σ_ω, and β can then be calculated by

$$\phi = F_1 \phi_1 + (1 - F_1) \phi_2 \tag{15}$$

Note that $\tilde{l}$ is the length scale:

$$\tilde{l} = \min(k^{1/2}/(\beta^* \omega), C_{\text{DES}} \Delta) \tag{16}$$

$$C_{\text{DES}} = (1 - F_1) C_1 + F_2 C_2 \tag{17}$$

Δ is the cube root of the cell volume. C_1 is 0.61, and C_2 is 0.78. Turbulent wall boundary conditions such as the k-q-R wall and ω wall functions are used at the injector plate, injector interfaces, and chamber wall.

C. Chemistry Model

The Westbrook–Dryer one-step global reaction with laminar kinetics is used to calculate the generation of species due to chemical reactions $\dot{\omega}_k$ and the heat release rate $\dot{\omega}_T$. No turbulent combustion closure is included. This approach was used to simulate the rocket engine combustor instability [25] and afterburner combustion problems [26].

This is the simplest chemical mechanism that requires only tracking four species: methane (CH_4), oxygen (O_2), carbon dioxide (CO_2), and water (H_2O). The rate of change of fuel mass fraction is given by

$$\frac{dY_{fuel}}{dt} = -\bar{A} Y_{fuel}^m Y_{ox}^n e^{(-E_a/R_u T)} \tag{18}$$

where CH_4 is the fuel, and O_2 is the oxidizer in the simulation. The chemical rate constants are $A = 8.3 \times 10^5 \ (g\,mol/cm^3)^{1-m-n}/s$, $m = -0.3$, $n = 1.3$, and $E_a = 30 \ k\,cal/g\,mol$. The generation of species is calculated using

$$\dot{\omega}_k = \rho \frac{dY_k}{dt} \tag{19}$$

The mass fractions are related to the other species using the chemical reaction equation

$$CH_4 + 2O_2 \Leftrightarrow CO_2 + 2H_2O \tag{20}$$
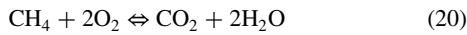
and molecular weights to give

$$\frac{dY_k}{dt} = \frac{MW_k}{MW_{CH4}} \frac{C_k}{C_{CH4}} \frac{dY_{CH4}}{dt} \tag{21}$$

C_k corresponds to the coefficient in front of each molecular species in Eq. (20). The heat source term due to chemical reactions is given by

$$\dot{\omega}_T = \sum_{k=1}^{NS} \dot{\omega}_k \left(h_0^f + \int_0^T C_{p,i}(s) \, ds \right) \tag{22}$$

D. Numerical Solver

In this study, the OpenFOAM is used to solve the governing equations. The differencing schemes used are second-order accurate in both space and time. The time discretization is second-order implicit backward differencing. Gaussian integration is used for the spatial discretization with linear interpolation from cell centers to cell faces for second-order derivatives. The rhoReactingFoam solver is used for the compressible combustion simulation with chemical reaction using a density-based thermodynamics package. The fuel CH_4 and oxidizer O_2 injection temperatures are 400 K. The critical
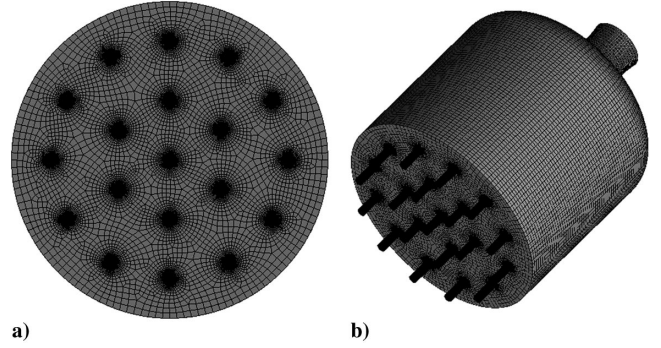

Fig. 1 The grid for 19-injector geometry with 43 cm chamber diameter and choked nozzle: a) front view; and b) isometric view.

temperatures for CH_4 and O_2 are $T_{CH_4} = 190.4$ K and $T_{O_2} = 154.6$ K, respectively. Thus, the injection temperatures of these propellants are above the critical values. And, the pressures and combustion-product temperatures in the combustion chamber are higher than the critical points of the gases. The ideal-gas state equation is used in this paper. The specific heat C_p is calculated as a function of temperature from the Joint Army Navy NASA Air Force tables of thermodynamics. The reacting-mixtures model is used to calculate the properties of the mixtures.

E. Computational Mesh

For both the 10- and 19-injector geometries, the fuel and oxygen were injected with coaxial injectors at a fixed mass flux (oxygen in the center, and fuel on the outside). Injector areas are chosen such that, given this mass flux, the mean velocity ratio between the fuel and oxygen is 2.28. For the 10-injector geometry, this resulted in $D_{ox} = 1.96$ cm and $D_{fuel} = 2.20$ cm. For the 19-injector geometry, this resulted in $D_{ox} = 1.42$ cm and $D_{fuel} = 1.61$ cm. The mass flux for each run is listed in Table 1. The combustion-chamber diameters are 28 and 43 cm. The length of the combustion chamber is 50 cm, and the distance between the injector plate and the choked nozzle is 33 cm for every case. The throat diameter for every run is also presented in Table 1. The grid is carefully generated to capture the burning of fuel in the mixing layer between the two coaxial streams. Figure 1 shows the 19-injector geometry with 43 cm chamber diameter and choked nozzle grid. The total number of grid points is about 3.8 million. The smallest size is about 0.03 cm/A. The number of points on the injector surface is about 4000.

A grid independency study has been performed for the 19-injector case with combustion chamber diameters of 43 and 28 cm. The total numbers of grid points of the fine meshes are about 7.5 million for the 19-injector geometry with 43 cm combustion chamber diameter and 10 million for the 19-injector with 28 cm combustion chamber diameter. The results show that overall qualitatively good grid independent solutions are achieved. The similar instability behaviors are captured on both coarse and fine meshes for the two 19-injector combustors. The predicted pressure oscillation frequencies by the coarse and fine meshes are almost identical. However, the flowfield reaches to the equilibrium state faster with the fine mesh, and more

Table 1 Test case parameters

	Injectors	D_c, cm	D_t, cm	$\dot{m}$, kg/s	ϵ	Instability mode	f, Hz	T_a, K	η_{CH4}, %
10A	10	28	9.5	80	0	None	——	3399	80.0
10B	10	28	8.2	65	0	Spontaneous longitudinal	1455.1	3540	86.6
10C	10	28	6.7	49	0	Spontaneous longitudinal	1596.3	4513	97.2
19A	19	28	9.5	80	0	Spontaneous longitudinal	1595.3	3916	84.5
19B	19	28	9.5	80	1.0	Spontaneous longitudinal	1622.7	3866	80.0
19LA	19	43	9.5	80	0	Spontaneous longitudinal	1437.0	3435	86.0
19LB	19	43	9.5	80	0.25	Triggered longitudinal	1448.0	3505	88.5
19LC	19	43	9.5	80	0.50	Triggered tangential	1771.4	4151	95.3
19LD	19	43	9.5	80	0.75	Triggered tangential	1796.5	4215	95.4
19LE	19	43	9.5	80	1.0	Triggered tangential	1807.5	4352	95.5
19LF	19	43	9.5	80	1.0	Triggered tangential	1803.5	4080	94.5

high-frequency noise is captured for the 19-injector geometry with a chamber diameter of 28 cm. To save computational costs, the coarse mesh is used for the rest of the simulation in the paper.

F.   Boundary Conditions

Along the wall, the no-slip boundary condition is used. The normal pressure gradient on the wall is zero. Adiabatic and no surface chemistry wall assumptions are used. At the inlet, the mean mass fluxes for methane and oxygen are fixed at the steady-state mass flow rate at the sonic point for the convergent nozzle. The temperature of the inflow fuel CH_4 and oxidizer O_2 is at 400 K and is injected at the stoichiometric ratio. The wave-transmissive boundary condition is used at the outlet boundary. This is due to the supersonic nature of the flow at the outlet. This boundary condition ensures that no backward-propagating waves enter the system and results in shocks or backflow.

III.   Computational Results

The simulations have been made for the 11 cases, which are listed in Table 1. The simulations start from an initially quiescent flow at 3000 K and an equilibrium chamber pressure at 200 bar. Because an explicit ignition model is not included in the current simulation, the higher chamber temperature helps to shorten the ignition process and reduce the computational time. For each case, the computational cost is about 306 CPU core hours per physical millisecond for an Intel Xeon E5-2650 V4 2.2 GHz machine.

To trigger the tangential and longitudinal instability modes for the 19-injector combustion chamber, the following pulsing injector mass flux is applied:

$$\dot{m} = \epsilon \dot{m}_0 \sin(2\pi f \times (t - t_0)) + \dot{m}_0 \qquad (23)$$

The pulsation begins at t_0 and stops after three cycles. Two different pulsation schemes are used in the present work, which are shown in Fig. 2. One is a traveling wave pulsation. A travelling wave is excited in the tangential direction by pulsing a pair of diametrically opposite injectors with the pulses 180 deg out of phase at every 1/12 pulsing period for the 12 injectors located at the outer ring of the injection plate. Essentially, the alignment of the pulsing pair of injectors rotates at the expected first tangential frequency. Another is the standing-wave pulsation. The outer rings of the 12 injectors are divided into two groups in different halves of the chamber. A standing wave is excited in the transverse direction by pulsing the two groups with the pulses 180 deg out of phase. The amplitude for each injector is proportional to the distance from the plane of antisymmetry for the standing wave. The pulsation frequency, which is an estimated first tangential mode, is calculated by

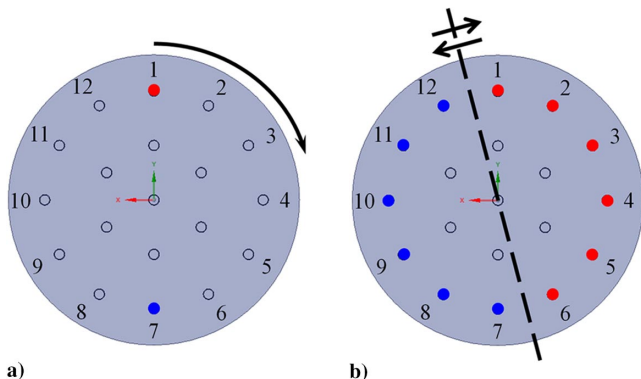$$f = \frac{k_r a}{2\pi} \qquad (24)$$

and

$$k_r = \frac{\alpha_{m,n}}{R} \qquad (25)$$

where $\alpha_{1,1} = 1.84$, and $a = \sqrt{\gamma R T}$. Also, ϵ is the pulsing mass-flux magnitude. T is the combustion-chamber temperature.

Here, in order to discover the responses for different external pulsing, four different pulsing mass-flux magnitudes are chosen: $\epsilon = 0.25$, $\epsilon = 0.5$, $\epsilon = 0.75$, and $\epsilon = 1.00$.

Table 1 presents the simulation results for the 11 cases. The instability mode is categorized, based only on the pressure oscillation type. For the 10-injector chamber, the self-excited longitudinal instability appears as the throat becomes smaller, and thereby the velocity in the combustion chamber is lowered with the increased residence time, leading to a greater combustion efficiency. The smaller throat area also permits less acoustic energy flow through the nozzle, which enhances the combustion instability. The longitudinal instability in turn enhances mixing, resulting in a higher fuel burning rate and a higher time-averaged chamber temperature. For the 19-injector geometry with a combustion-chamber diameter equal to 28 cm, only longitudinal instability is observed for the cases with and without the inlet mass-flux traveling wave pulsation. The inlet pulsation, however, causes the longitudinal instability to start earlier. The 10- and 19-injector chambers with 28 cm diameter combustion simulation results indicate that the combustion tends to become more efficient and more unstable as the number of injectors increase. The smaller diameter chamber cannot sustain the tangential instability wave development; so, only a longitudinal instability wave is observed. Although, for the 19-injector geometry with a larger-diameter 43 cm combustion chamber, multiple solutions are observed for different inlet mass-flux excitations. The 43 cm combustion chamber yields a frequency of the first tangential mode close to the frequency of the first longitudinal mode for the 28 cm (and 43 cm) combustion chamber. This implies a Crocco time-lag effect [2,4,5,7,8]. The detailed simulation results are analyzed in the following sections.

A.   Combustion Flowfield Analysis

In this section, the simulation results of the 43-cm-diameter combustion-chamber cases are discussed. To trigger the tangential instability, various magnitudes of the inlet mass-flux traveling wave pulsation are used for cases 19LB–19LE with different magnitudes. The inlet mass-flux standing-wave pulsation is used for case 19LF. For every case, the pulsation begins at $t_0 = 10$ ms with a frequency of 1502.5 Hz, calculated by Eq. (24), and stops after three cycles. Figure 3 shows the pressure history at a point on the combustion-chamber wall 1.0 cm downstream from the injection plate for cases 19LA, 19LB, and 19LE. For case 19LA without pulsation, the pressure inside the combustion chamber stays around 210 bar with minor oscillations. The peak-to-peak pressure fluctuation is about 1% of the mean value. For case 19LB, a $\epsilon = 0.25$ magnitude inlet mass-flux pulsation is applied. When the moderate pulsation is applied at 10 ms, the pressure starts to oscillate with small amplitude. The oscillation amplitude gradually grows up to about 2% of the mean pressure. When the strong $\epsilon = 1.00$ magnitude inlet mass-flux pulsation is applied, the pressure starts to oscillate with large amplitude and the mean pressure quickly increases to a higher value. The large pressure oscillation enhances the flow mixing and the burning rate. The higher burning rate increases the temperature and pressure inside the combustion chamber with a fixed total mass flow rate. After a long run time, the mean pressure inside the chamber reaches about 230 bar and the peak-to-peak pressure fluctuation is about 20% of the mean value.

To examine the instability mode type of the combustion, we place six pressure probes on the combustion-chamber wall 28 cm downstream of the injection plate, and they are evenly distributed around the wall with 60 deg intervals.

Figure 4 shows the pressure history of the last 10 ms of the simulation on the combustion-chamber wall. For case 19LA, the pressure fluctuations are small and the pressure fluctuations at the six positions are all in phase. Thus, the spontaneous longitudinal instability mode is obtained. For case 19LB, with the moderate inlet

Fig. 2   Pulsation schemes: a) travelling wave pulsation; and b) standing-wave pulsation. (Red indicates positive, and blue indicates negative.)
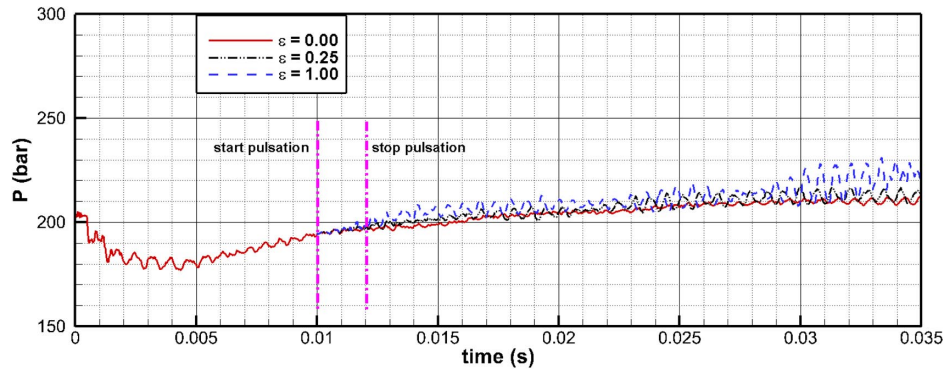
Fig. 3 Pressure history on the combustion-chamber wall ($z = 1$ cm).

mass-flux pulsation, the pressure fluctuations are higher than case 19LA. But, the pressure fluctuations at the six positions are still all in phase. The triggered longitudinal instability mode is obtained for this case. When the pulsation magnitude is greater than 0.50, the tangential instability mode is triggered. The pressure oscillation amplitude is significantly increased to about 20% of the mean value. The pressure fluctuations at the six positions around the wall are 60 deg out of phase, which is evidence of the tangential instability mode. The pressure histories show similar behavior of cases 19LC–19LE, and so only the 19LE case is presented in Fig. 4. When the standing-wave pulsation is used for case 19LF, the triggered tangential instability mode is also observed. Although the pressure histories show similar patterns in cases 19LE and 19LF, there are still some differences with the mean pressure, the oscillation frequency, the mean temperature, and the mean fuel burning rate between them. For the nonlinear dynamic system, different solutions and different instability modes could be triggered by different inlet mass-flux excitations.

From the pressure history analysis, two different types of combustion instability modes (longitudinal and tangential instabilities) are observed. So, two cases (19LB and 19LE) are chosen to investigate the flow behaviors of the two types of the combustion instability. The flow behaviors of other simulations are similar to these two cases.

Figures 5–7 show the time-averaged fuel mass fraction, the heat release rate (HRR), and the temperature in the $x = 0$ cm meridian plane of the 19LB and 19LE cases with the time duration covering 12 oscillation periods.

For case 19LB, the small pressure oscillation cannot mix the fuel and oxidizer well when they are injected into the combustion chamber. Near the center of the combustion chamber, the burning does not begin immediately at the injector exit but starts, rather, about five injector diameters downstream of the injector at $z \approx 11$ cm. So, the fuel mass fraction near the center of the combustion chamber remains high upstream near the injectors until the burning starts downstream. Near the combustion-chamber wall, the burning starts further upstream and the fuel mass fraction is therefore reduced sharply. Further downstream, near the middle of the combustion chamber where the node exists for the longitudinal instability pressure wave, the burning rate is relatively low. With the low burning rate, the fuel mass fraction only has a very small change at the middle of the combustion chamber. The propellants injected from adjacent injectors start to mix together. Near the nozzle entrance where the antinode exists for the longitudinal instability pressure wave, the pressure oscillation reaches a maximum, which helps to mix the fuel and oxidizer and enhance burning. So, the strong burning also occurs near the nozzle entrance, which causes a large change of the fuel mass fraction. Overall, the pressure oscillation is only about 2% of the mean value and the combustion is relatively stable. The fuel burning rate is relatively low, and some unburned propellants emit from the nozzle. With the lower burning rate of 88.5%, the propellants are not consumed rapidly and some cold propellants flow downstream with the jets, which results in a lower time-averaged temperature of 3505 K inside the combustion chamber.

For case 19LE, the triggered strong tangential instability induces a larger pressure amplitude, which is about 20% of the mean value of the combustion chamber and significantly enhances the mixing of the fuel and oxidizer injected into the combustion chamber. The propellants injected from adjacent injectors begin to mix together near the exit of the injectors. The higher mixing rate causes a higher burning rate. The burning starts very close to the injector. The fuel mass fraction is quickly reduced to a low level. And, the burning is nearly completed before the flow reaches the nozzle. The burning efficiency is about 95.5%. Because of the high burning rate and that the propellants are consumed more rapidly, the cold jet flow does not extend far; so, a higher time-averaged temperature of 4352 K is reached inside the combustion chamber.

Figure 8 shows instantaneous Mach number contour in the $x = 0$ meridian plane of the combustion chamber and choked nozzle for the 19LE case. The area-averaged Mach number in the throat plane is slightly lower than the sonic value. Near the center of the throat plane, the Mach number is about 0.96. The Mach number gradually increases to one from the center to the higher radius region, and then it decreases to zero on the nozzle wall. The nonuniform distribution of the Mach number in the throat plane is caused by the viscous effects. The sonic plane in the nozzle is distorted to a curved surface. The Mach number in the outlet is about 1.3, which indicates the flow is supersonic downstream of the throat and the information will not propagate upstream. The supersonic flow is always achieved in the divergent part of the nozzle for any other instantaneous time. The supersonic Mach number certifies the flow is choked in the system. For other test cases, the flow is also always choked.

B. Mechanism for Combustion Instability

To further understand the two instability mechanisms, the instantaneous flowfields are examined for cases 19LB and 19LE.

To remove any phase-lag bias due to the spatial location of the signals, the volume-averaged method is used [14]. For this case, the volume that is used for the average only contains half of the combustion chamber between the injection plate and the entrance of the attached nozzle along the streamwise direction. Figures 9 and 10 show the volume-averaged pressure, the heat release rate, and the vorticity magnitude history of last 10 ms for case 19LB. As seen in Fig. 9, the heat release rate is almost in phase with the slightly lagging pressure oscillation for the longitudinal instability. The vorticity magnitude oscillation frequency is the same as the pressure oscillation frequency. However, the vorticity magnitude oscillation is about 90 deg out of phase with the pressure oscillation. Figure 11 shows the pressure signal of the last 10 ms of the calculation along the centerline of the combustion chamber. There is a large pressure oscillation in the injector coupled that sustains the pressure oscillation inside the combustion chamber. The pressure oscillations in the injector and chamber have the same frequency but are in opposite phases. The pressure oscillations inside the exit nozzle are smaller and in phase with the pressure oscillation inside the combustion chamber. Inside the combustion chamber, there are two antinodal points: one near the exit of the injector and the other near the entrance of the nozzle. And, the nodal point is at the middle of the combustion chamber. The pressure oscillation is not strong enough to form a shock wave.
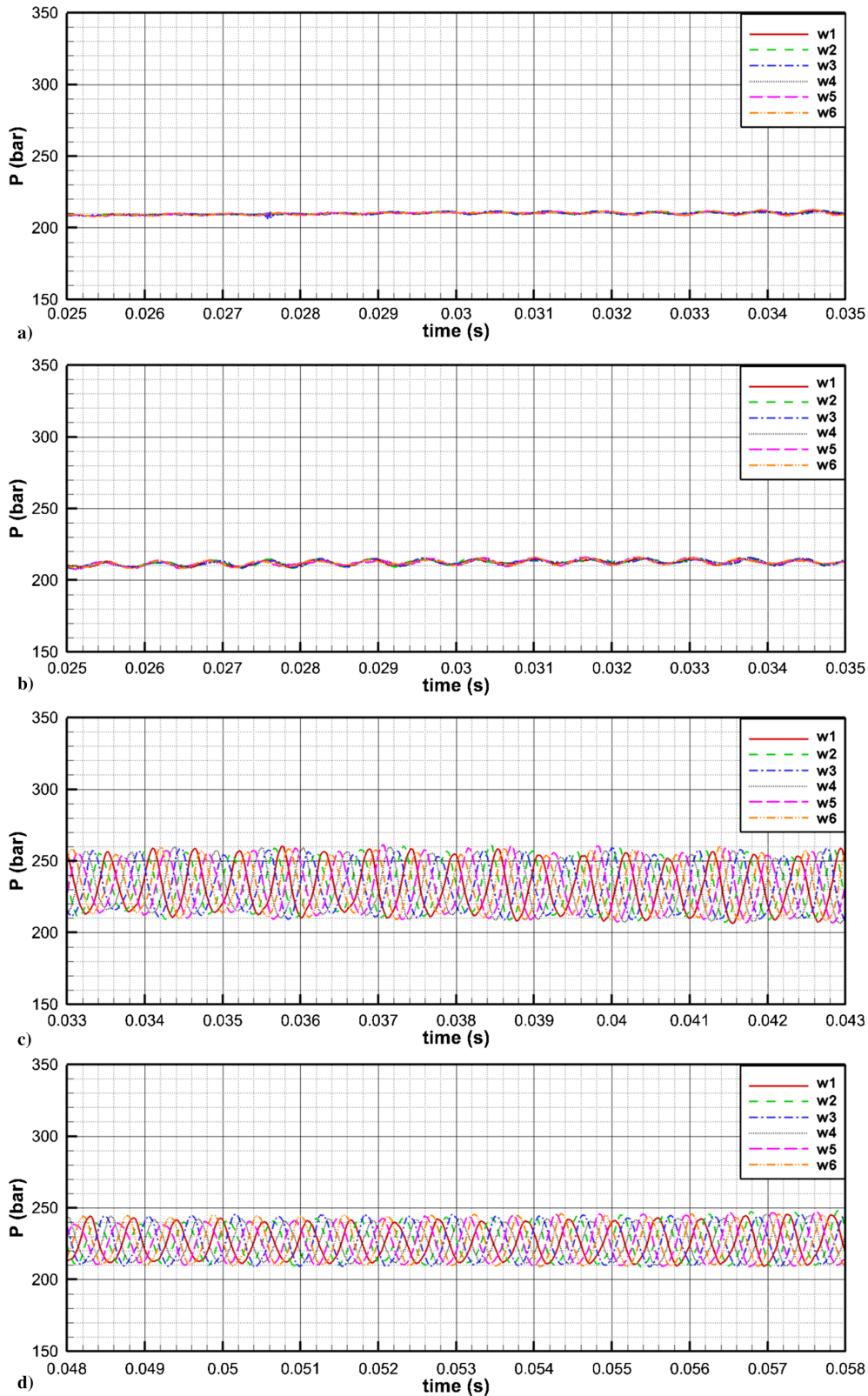
Fig. 4   **Pressure history on the combustion-chamber wall: a) 19LA ($\epsilon = 0.0$); b) 19LB ($\epsilon = 0.25$); c) 19LE ($\epsilon = 1.0$); and d) 19LF ($\epsilon = 1.0$).**

Figures 12–14 show the instantaneous pressure deviation, the heat-release-rate deviation, and the helicity $\mathbf{\Omega} \cdot \mathbf{U}$ (the dot product of the vorticity and velocity, which is an indicator of streamwise vorticity) contours in the $x = 0$ meridian plane of the combustion chamber during one cycle for case 19LB. During one cycle, the pressure wave sweeps back and forth through the combustion chamber. At time $T/4$, the pressure disturbances are close to zero inside the chamber, but the pressure disturbances in the injectors reach the positive maximum. At

time $T/2$, the pressure disturbances reach a maximum near the nozzle entrance, a negative maximum near the injector, and near zero at the middle of the combustion chamber. The pressure disturbances in the injector ports are reduced. The locations of both the peak pressure and the peak heat release rate occur about five injector diameters downstream of the injector and near the entrance of the nozzle. The two separate unstable regions in the combustion chamber oscillate out of phase. The helicity contours show that, near the exit of the
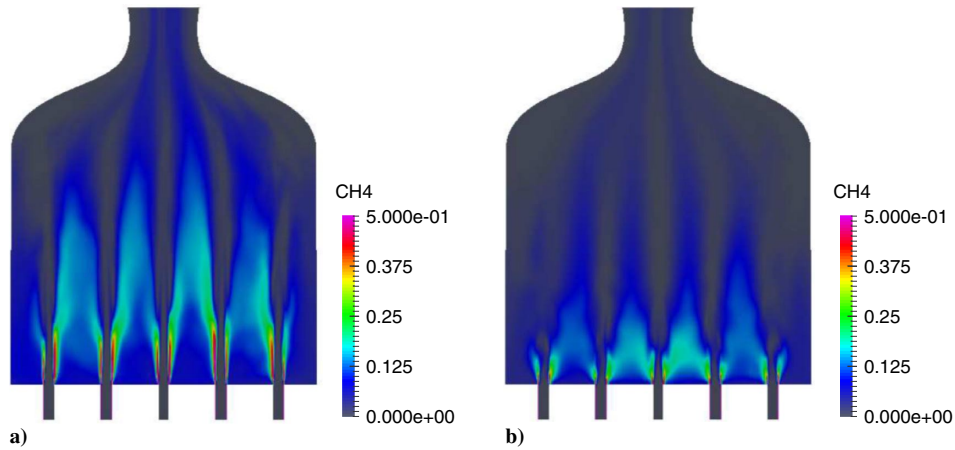
Fig. 5   Time-averaged fuel CH$_4$ mass fraction in the combustion-chamber x plane ($x = 0$ cm): a) 19LB; and b) 19LE.
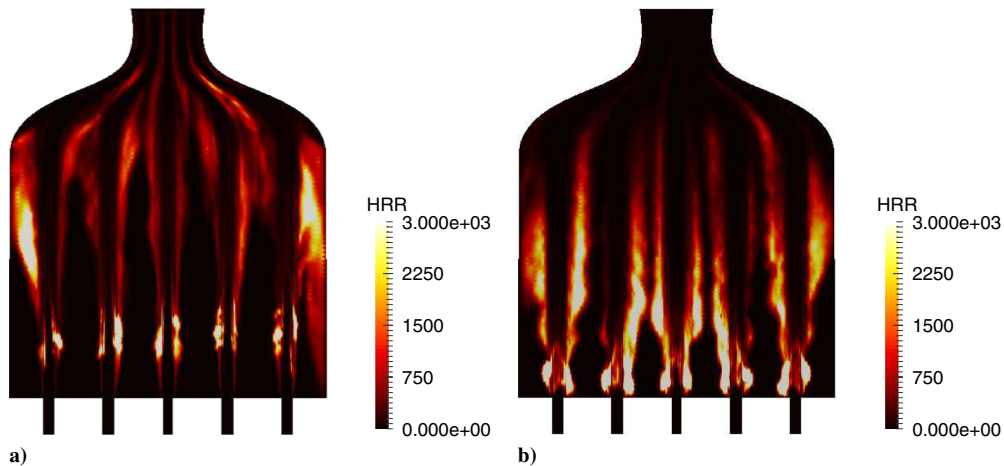
Fig. 6   Time-averaged HRR in the combustion-chamber x plane ($x = 0$ cm): a) 19LB; and b) 19LE.
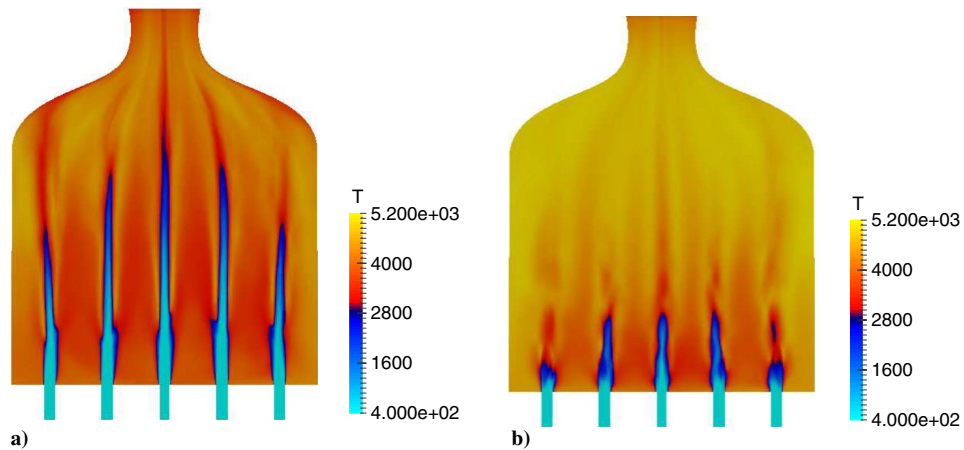
Fig. 7   Time-averaged temperature in the combustion-chamber x plane ($x = 0$ cm): a) 19LB; and b) 19LE.

injector, the mean flow is more stable hydrodynamically and more like a laminar flow. The mixing is not strong in this region. At about five injector diameters downstream of the injector, at $z \approx 11$ cm, the vortices begin roll up, which enhances mixing. Then, the burning occurs near this region. At the middle section of the combustion chamber, although the vortices help to mix the gases, the burning rate is still low due to weak pressure oscillation at the nodal point. Near the entrance of the nozzle, the strong burning occurs again. At time $3T/4$, the pressure disturbances are close to zero again inside the chamber, but the pressure disturbances in the injectors reach the negative maximum. The heat release rate and vortex patterns change little. At time T, the pressure disturbances near the nozzle entrance reach the

negative maximum. The pressure disturbances about five injector diameters downstream of the injector reach the positive maximum. However, the heat release rates become weak about five injector diameters downstream of the injector. At the middle of the combustion chamber, the pressure disturbance is still close to zero and the heat release rate is relatively weak. Little spatial or temporal correlation of the streamwise vorticity with the pressure wave is seen. Near the nozzle entrance, the spatial pressure oscillations are observed, which are caused by the rapid flow contraction. They indicate a continual stream of short wavelength kinematic waves with varying temperatures and vorticities is reaching the throat, and thereby affecting the allowable mass flow.
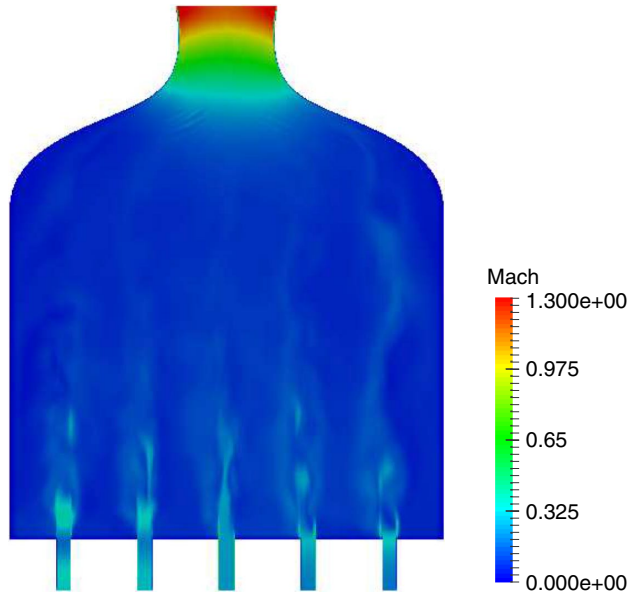
Fig. 8 **Instantaneous Mach number contour in the chamber x plane ($x = 0$) for case 19LE.**

Fig. 11 **Pressure history along the centerline for case 19LB.**

Figures 15 and 16 show the volume-averaged pressure, the heat release rate, and the vorticity magnitude for case 19LE. For this case, the volume contains one half of the combustion chamber on one side of a meridian plane and between the injection plate and the entrance of the attached nozzle. As seen in Fig. 15, the heat release rate is completely in phase with the pressure oscillation, which results in the strong tangential instability. The vorticity oscillation frequency is the same as the pressure oscillation frequency and is in phase with the pressure oscillation, which should further enhance the instability through the mixing process. Figure 17 shows the pressure signals along the combustion-chamber upper wall ($y = 14$ cm, $x = 0$ cm) and lower wall ($y = -14$ cm, $x = 0$ cm) at different times. There is

also a large pressure oscillation in the injector that can sustain the pressure oscillation inside the combustion chamber through mass flow. Under the tangential instability mode, the system displays a coupled mode between the oxidizer feed system and the combustion chamber. The pressure oscillations in the injector and chamber have the same frequency but are exactly 180 deg out of phase. The pressure wave strength becomes weaker when the flow enters into the nozzle.

Figures 18–23 show the instantaneous pressure deviation, the heat-release-rate deviation, and the helicity contours in the $x = 0$ meridian plane and the $z = 1$ cm cross-sectional plane of the combustion chamber during one cycle for case 19LE. The $z = 1$ cm cross-sectional plane is taken in the mainstream direction looking from the injector toward the nozzle. At time $T/4$, the pressure disturbances on the combustion-chamber left side reach the positive maximum. The pressure disturbances on the combustion-chamber right side reach the negative maximum. The fluctuations gradually decrease from the chamber wall to the center of the chamber, which is standard for the fluid tangential mode. The heat-release-rate deviation and the
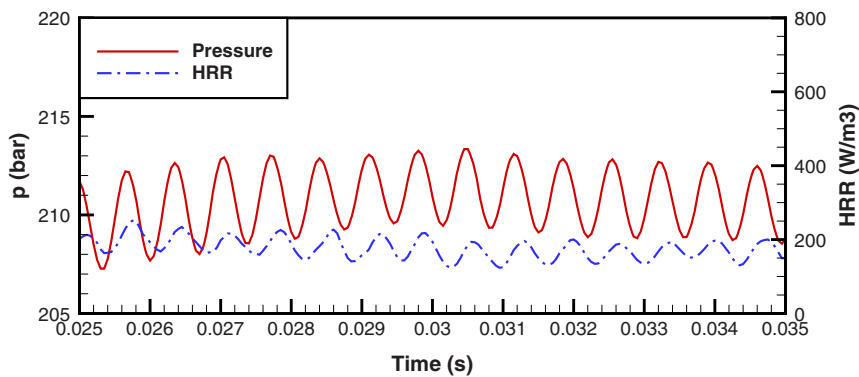

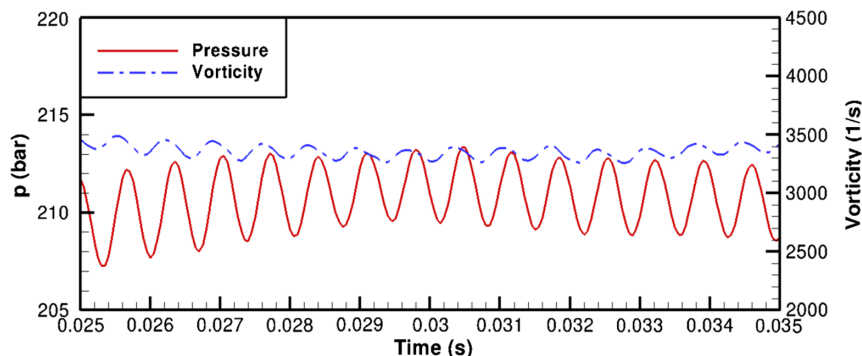**Fig. 9** **Volume-averaged pressure and heat release rate for case 19LB.**

Fig. 10 **Volume-averaged pressure and vorticity magnitude for case 19LB.**
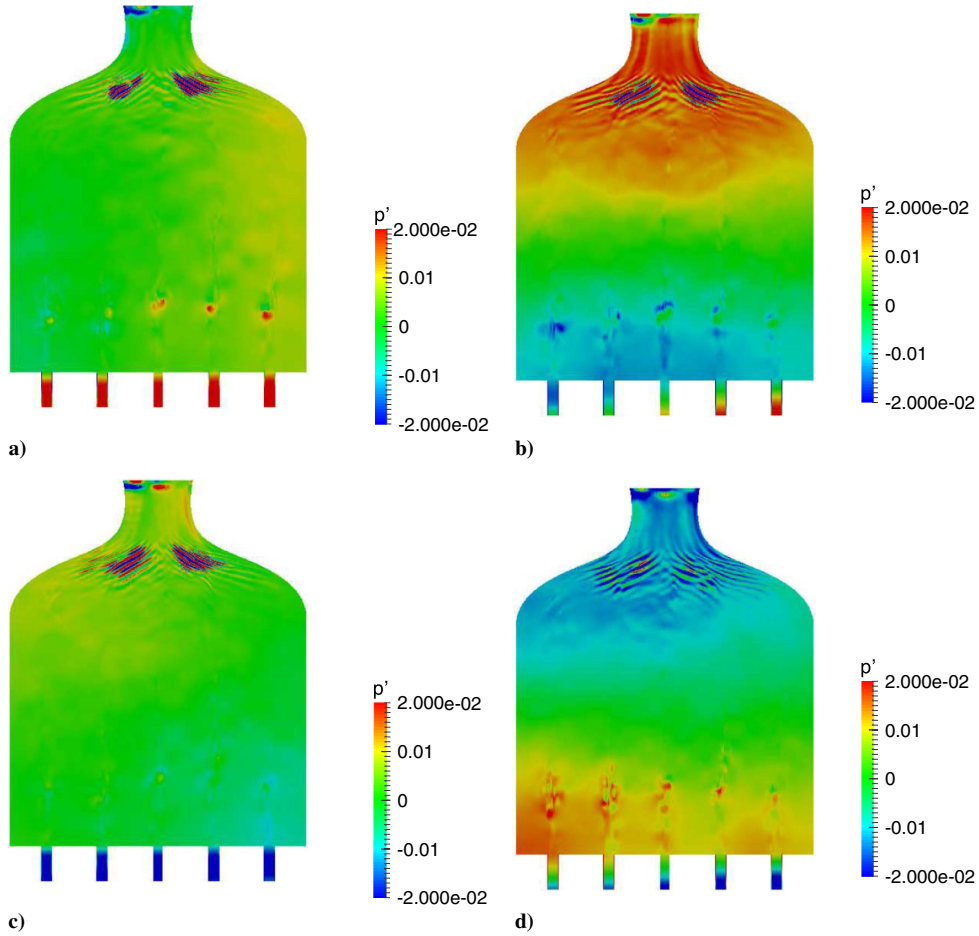
Fig. 12 Instantaneous pressure deviations in the chamber x plane ($x = 0$) for 19LB: a) $t = 1/4$ T; b) $t = 1/2$ T; c) $t = 3/4$ T; and d) $t = T$.
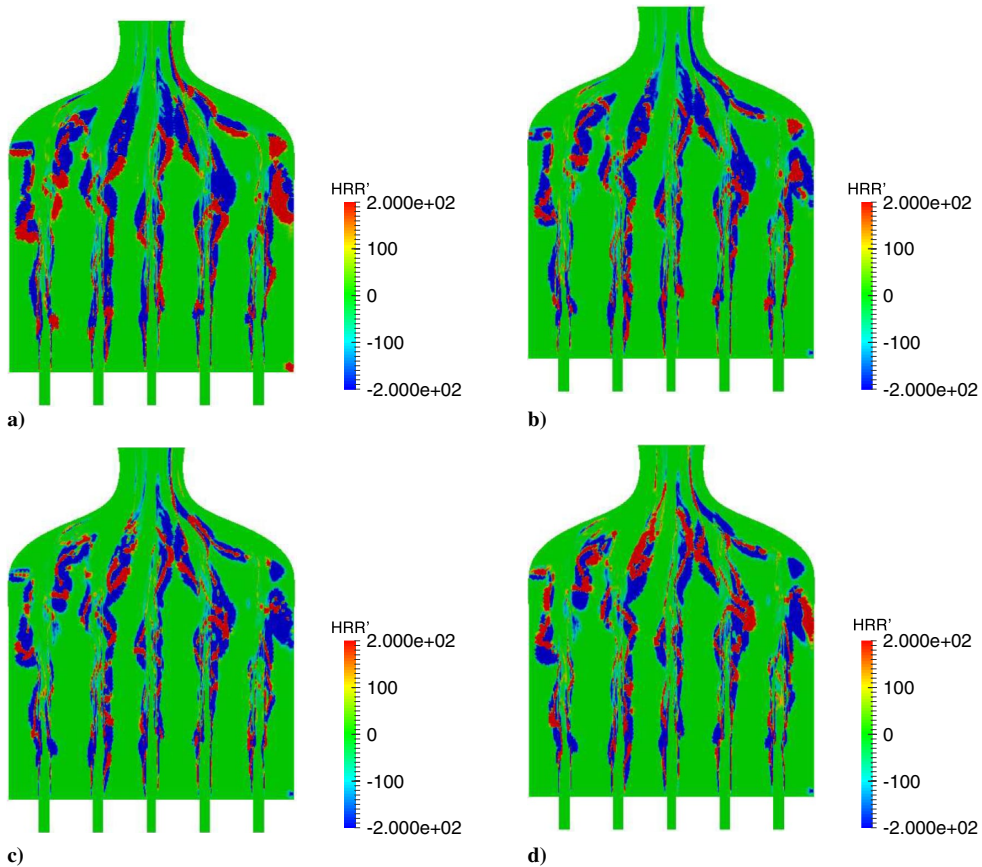

Fig. 13 Instantaneous HRR deviations in the chamber x plane ($x = 0$) for 19LB: a) $t = 1/4$ T; b) $t = 1/2$ T; c) $t = 3/4$ T; and d) $t = T$.
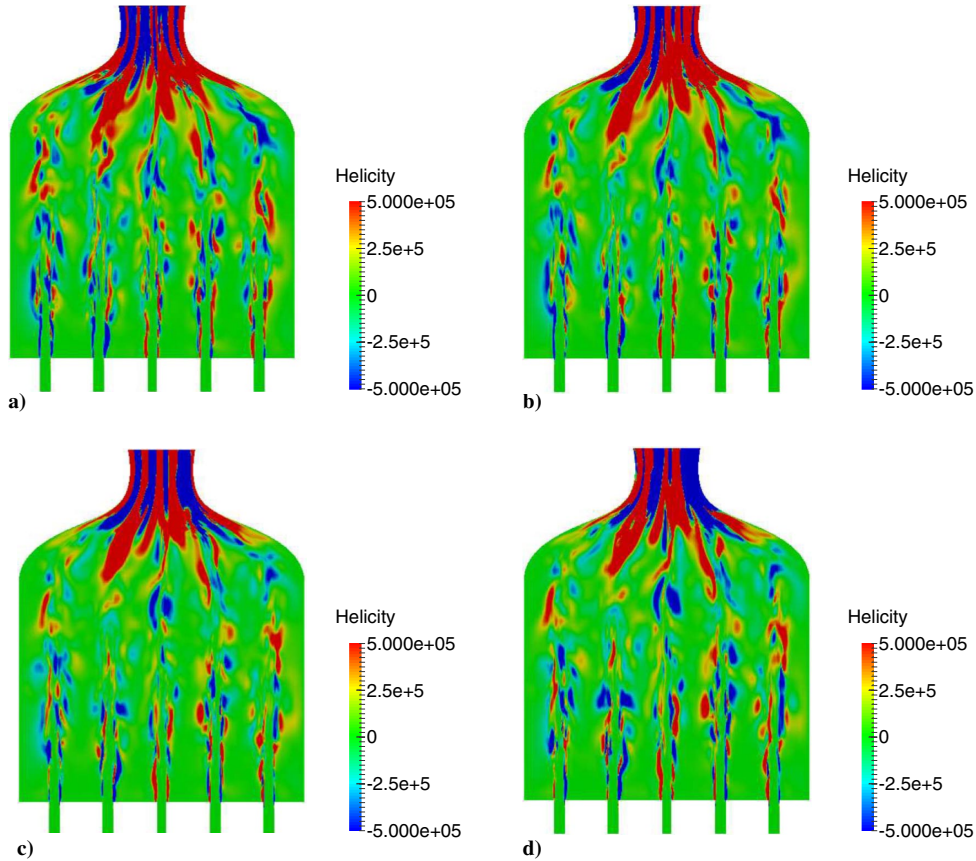
Fig. 14   Instantaneous helicities in the chamber x plane ($x = 0$) for 19LB: a) $t = 1/4$ T; b) $t = 1/2$ T; c) $t = 3/4$ T; and d) $t = T$.
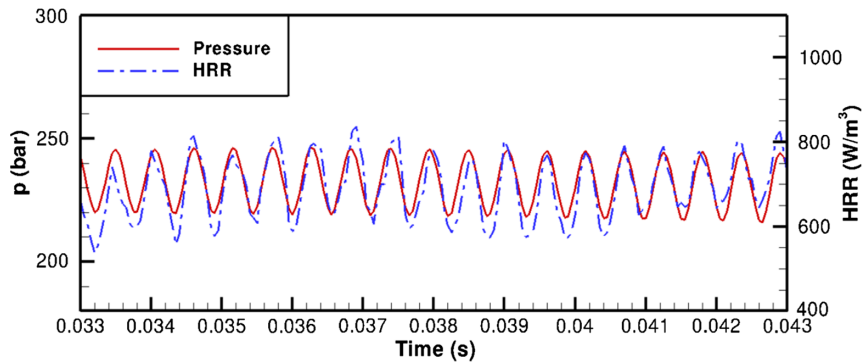

Fig. 15   Volume-averaged pressure and heat release rate for case 19LE.
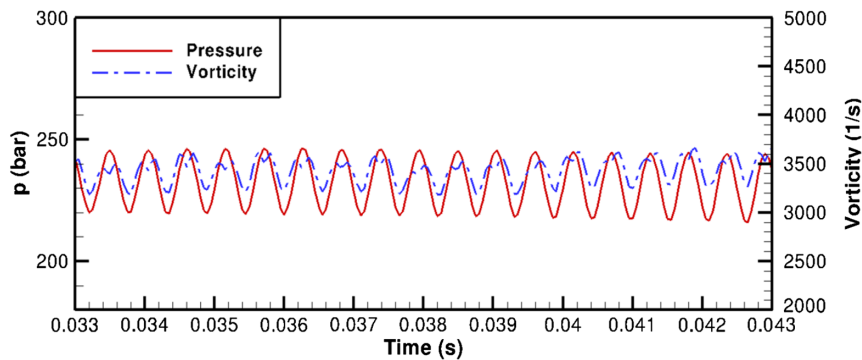
Fig. 16   Volume-averaged pressure and vorticity magnitude for case 19LE.

streamwise vorticity are positive on the left side relative to each local injector. And, the heat-release-rate deviation and the streamwise vorticity are negative on the right side relative to each local injector. The strong coupling between the pressure wave, the heat-release-rate

wave, and the streamwise vorticity will induce strong instability. The pressure disturbances in the injectors are out of phase with the pressure disturbances inside the combustion chamber. At time $T/2$, the pressure wave rotates about 90 deg in the clockwise direction
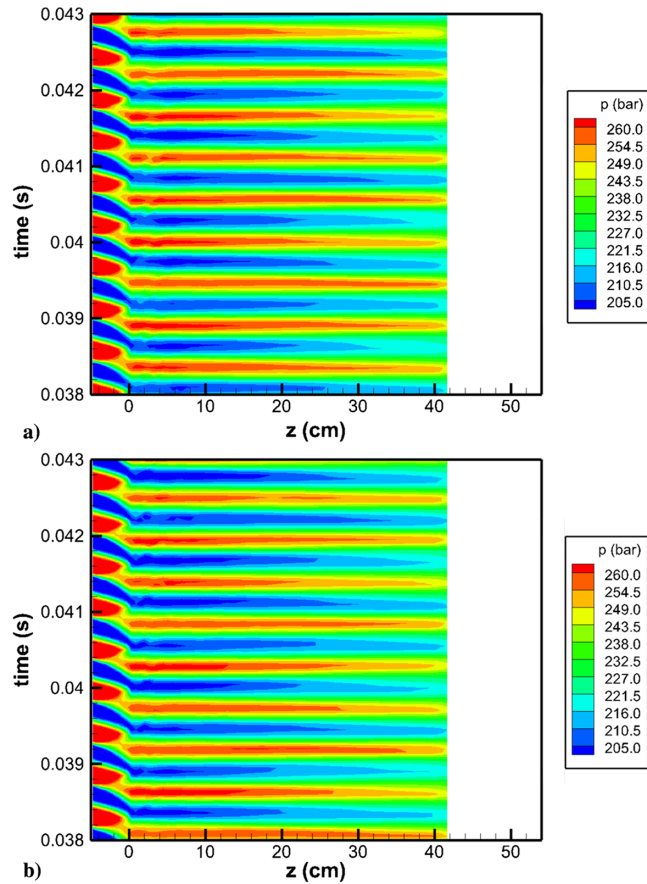
Fig. 17 Pressure history along the chamber wall for case 19LE: a) upper wall ($y = 14$ cm, $x = 0$ cm); and b) lower wall ($y = -14$ cm, $x = 0$ cm).
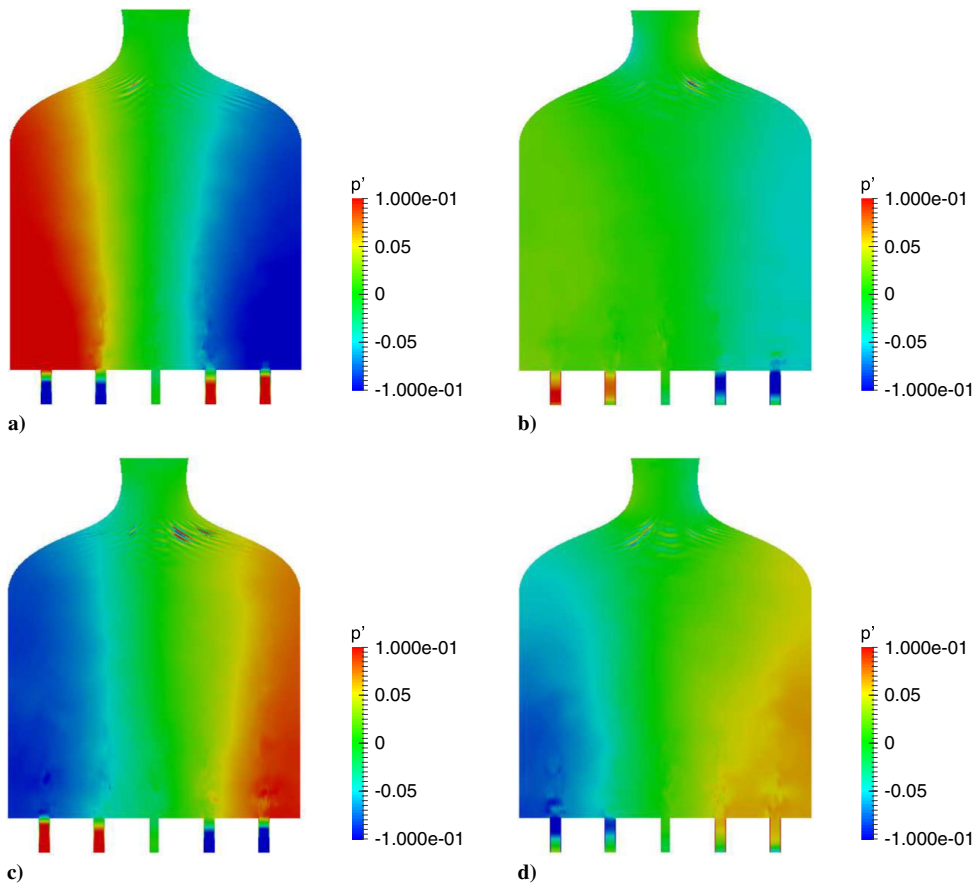

Fig. 18 Instantaneous pressure deviation on the chamber x plane ($x = 0$) for 19LE: a) $t = 1/4$ T; b) $t = 2/4$ T; c) $t = 3/4$ T; and d) $t = 4/4$ T.
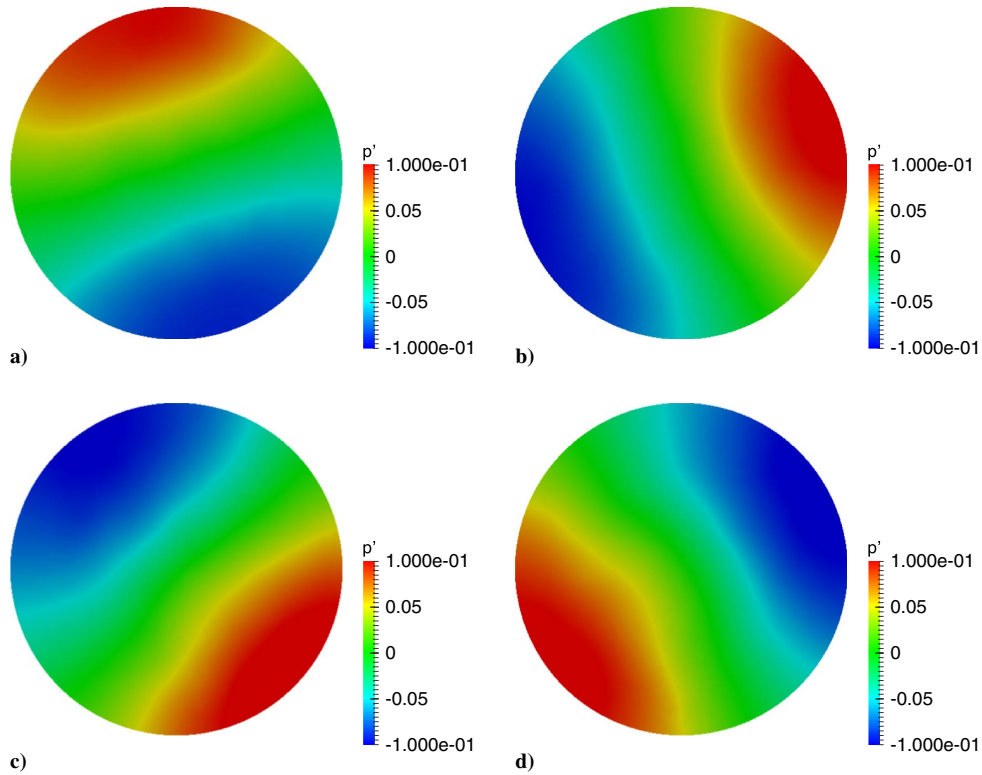
Fig. 19 Instantaneous pressure deviation on the chamber z plane ($z = 1$ cm) for 19LE: a) $t = 1/4$ T; b) $t = 2/4$ T; c) $t = 3/4$ T; and d) $t = 4/4$ T.
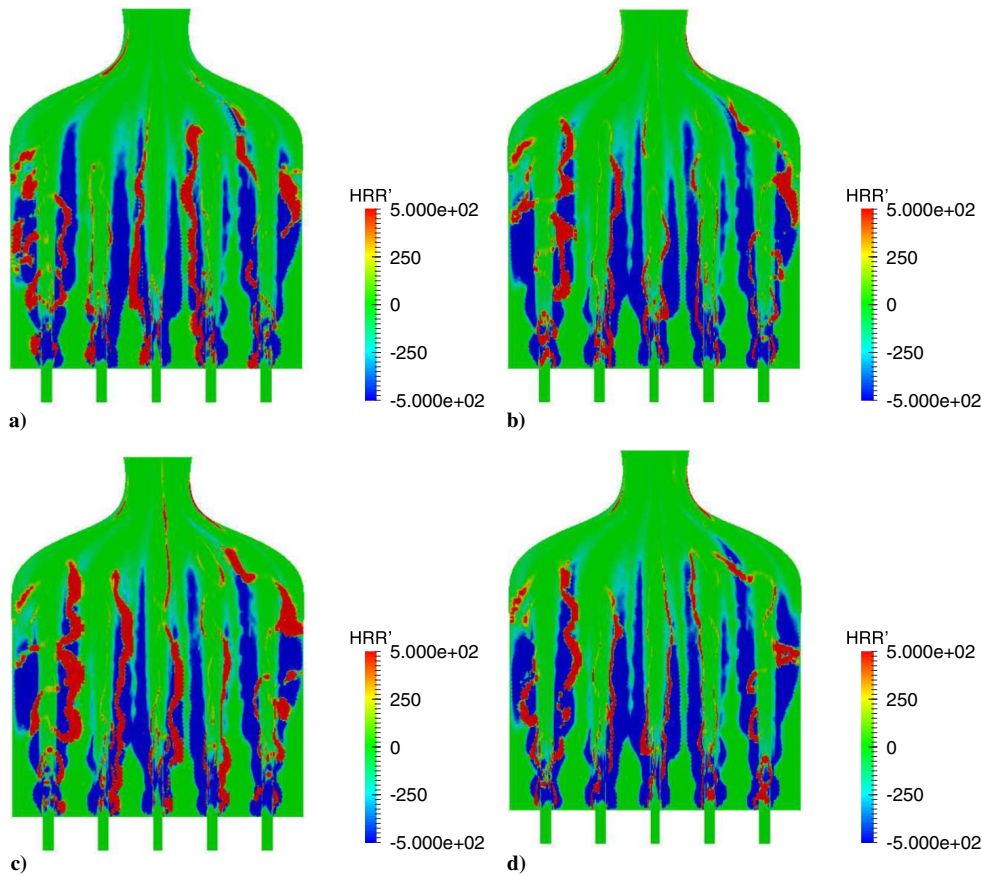

Fig. 20 Instantaneous HRR deviation on the chamber x plane ($x = 0$) for 19LE: a) $t = 1/4$ T; b) $t = 2/4$ T; c) $t = 3/4$ T; and d) $t = 4/4$ T.

around the combustion chamber. Similarly, the heat-release-rate wave and the streamwise vorticity wave rotate about 90 deg in the clockwise direction around each local injector. At time $3T/4$, the pressure disturbances distributions in the combustion chamber and

injector are opposite compared to those at time $T/4$. The pressure disturbances on the combustion-chamber left side reach the negative maximum; the pressure disturbances on the combustion-chamber right side reach the positive maximum. The heat-release-rate wave
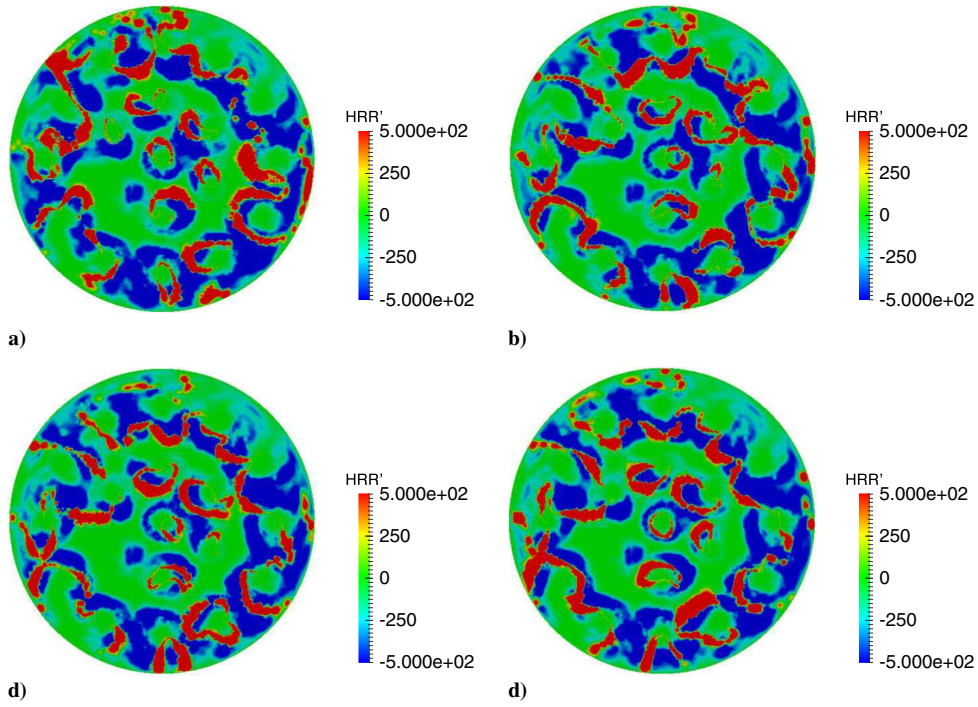
Fig. 21   Instantaneous HRR deviation on the chamber z plane ($z = 1$ cm) for 19LE: a) $t = 1/4$ T; b) $t = 2/4$ T; c) $t = 3/4$ T; and d) $t = 4/4$ T.
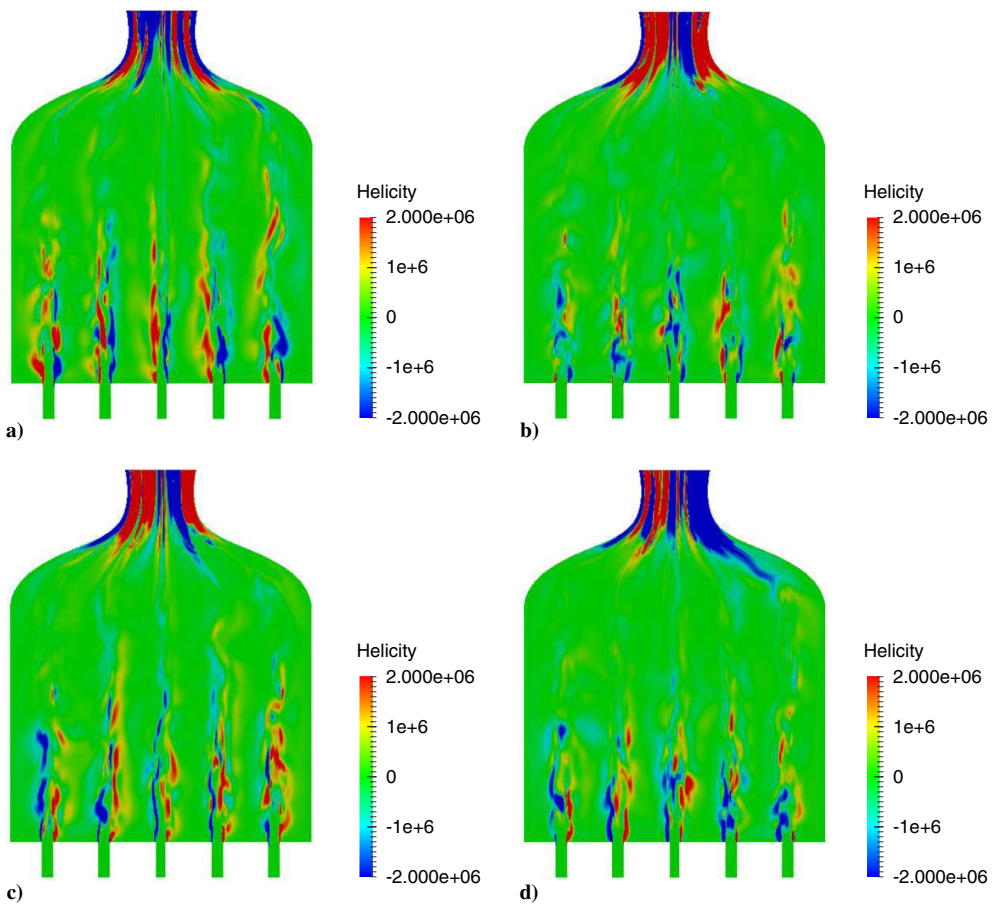

Fig. 22   Instantaneous helicity on the chamber x plane ($x = 0$) for 19LE: a) $t = 1/4$ T; b) $t = 2/4$ T; c) $t = 3/4$ T; and d) $t = 4/4$ T.

and the streamwise vorticity wave rotate around each local injector, in phase with the pressure wave, which further enhances the tangential instability. At time T, the pressure disturbances, the heat-release-rate deviation, and the streamwise vorticity in the combustion chamber

are opposite in sign as compared to their values at time $T/2$. During one cycle, the pressure wave rotates around the combustion chamber, in phase with the heat release wave and the streamwise vorticity wave. Figure 24 shows the instantaneous projected velocity vectors around
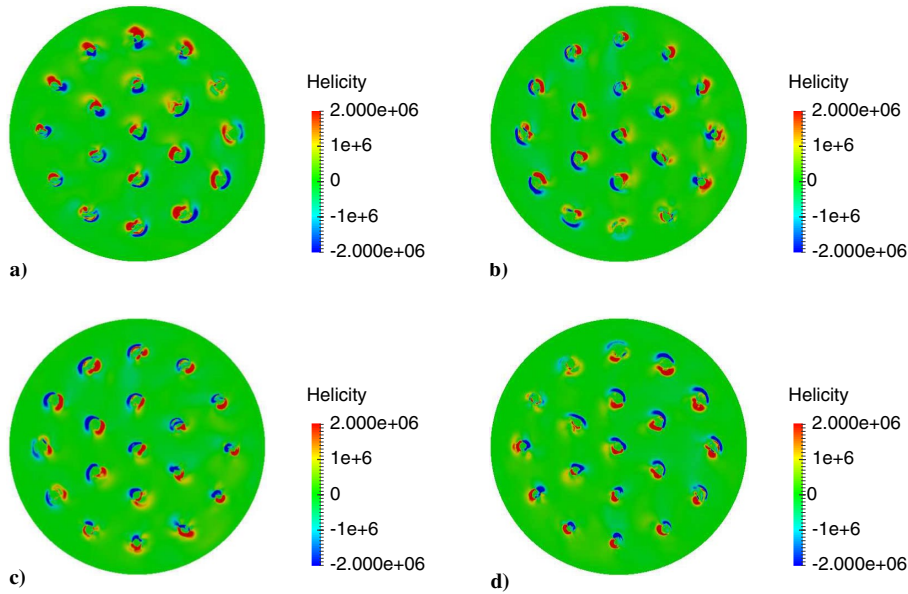
Fig. 23   Instantaneous helicity on the chamber x plane ($z = 1$ cm) for 19LE: a) $t = 1/4$ T; b) $t = 2/4$ T; c) $t = 3/4$ T; and d) $t = 4/4$ T.
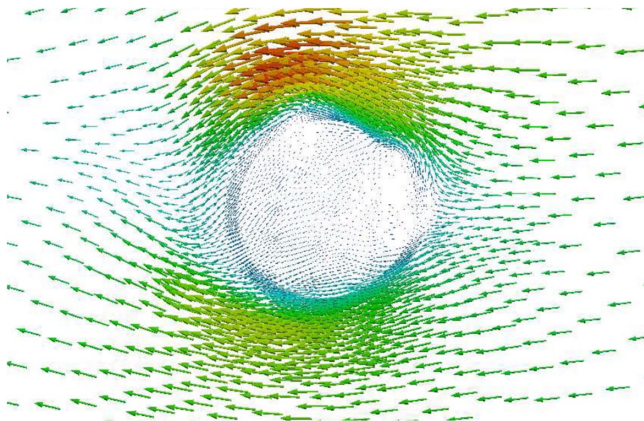

Fig. 24   Instantaneous velocity vectors in the chamber z plane ($z = 1$ cm) for 19LE.

injector no. 1 in Fig. 2 in the chamber transverse plane 1 cm downstream from the injection plate. The acoustically driven transverse flow in the combustion chamber shears and displaces the axial jet flow and initiates internal circulation in the transverse plane of the injector jet flow. The coupling between the pressure wave, the heat release wave, and the streamwise vorticity wave induces the strong instability, which results in a large pressure oscillation, as well as a higher mixing rate and burning rate.

C.   Rayleigh Index

To study the interaction between acoustic waves and flames, the Rayleigh index is used. The Rayleigh index provides a measure of the power fed by combustion to the acoustics field. The time-averaged spatially local Rayleigh index (RI) [15,27] is defined as follows:

$$\text{RI} = \frac{1}{p_a \tau} \int_{t_0}^{t_0+\tau} \frac{\gamma}{\gamma - 1} p' \dot{\omega} \, \text{d}t \qquad (26)$$

where τ is the period of the instability, p' is the local pressure oscillation, p_a is the local time-averaged pressure, and $\dot{\omega}$ is the local heat-release-rate oscillation. It provides the information about the pressure and heat-release-rate coupling mechanism. If the pressure oscillates in phase with heat release rate, the flow is more likely to be unstable. If they are out of phase, stability is more likely. The Rayleigh index has been calculated for the cases 19LB and 19LE. And, the values are averaged over the last 5 ms of the simulation.

Figures 25 and 26 show the time-averaged Rayleigh index in two planes of the combustion chamber for cases 19LB and 19LE. For the 19LB case, the values of the Rayleigh index are small. The distribution of the Rayleigh index shows that there are two high value zones: one at five injector diameters downstream, and the other near the nozzle entrance. The two zones coincide with the fuel burning locations. In the middle of the chamber, the values of the Rayleigh index are close to zero, which means there are very small pressure and heat-release-rate oscillations in that region. That is caused by two longitudinal instability waves sweeping back and forth through the
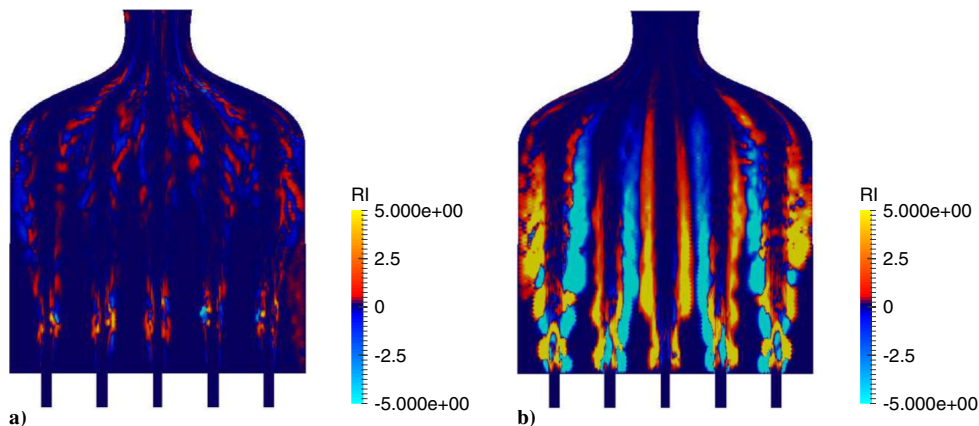

Fig. 25   Time-averaged Rayleigh Index on the combustion-chamber x plane ($x = 0$): a) 19LB; and b) 19LE.
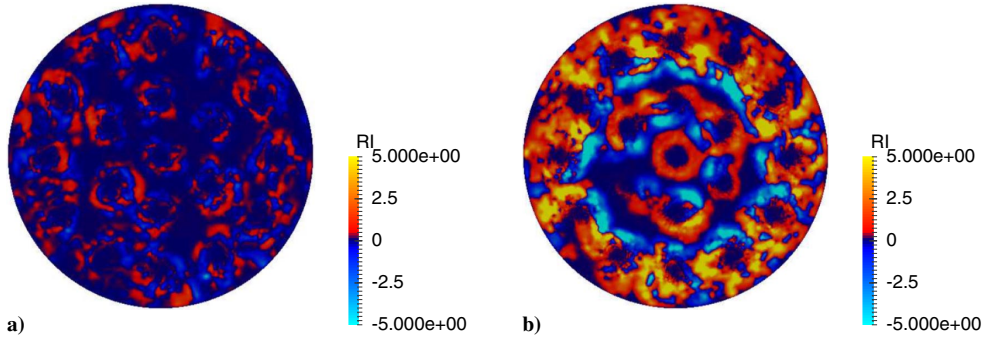
Fig. 26 Time-averaged Rayleigh Index on the combustion-chamber z plane ($z = 28$ cm): a) 19LB; and b) 19LE.

Table 2 Injector-size scaling

	Injectors	Mixture ratio (oxygen/fuel)	Instability mode	f, Hz	K, m/(m/s)^n	n	ΔU, m/s
10D	10	4:1	Spontaneous longitudinal	1580.5	$2.916E - 05$	1.25	170.0
19A	19	4:1	Spontaneous longitudinal	1595.3	$2.916E - 05$	1.25	141.5
10E	10	4:1.1	Spontaneous longitudinal	1610.0	$2.436E - 05$	1.25	196.3
19C	19	4:1.1	Spontaneous longitudinal	1596.1	$2.434E - 05$	1.25	163.4

chamber, and the middle section of the chamber is the nodal point. For the 19LE case, the values of the Rayleigh index are large, which is associated with the large amplitude of the fluctuations. The spinning tangential instability wave travels around the chamber and makes the large positive Rayleigh index region extend all through the chamber. And, the maximum positive Rayleigh index region appears in the outer regions near the chamber wall.

D. Injector-Size Scaling Effects

In this section, a preliminary analysis of injector-size scaling effects is given. Here the 10- and 19-injector chambers with 28 cm diameters are tested. In addition to matching the mass flow rate, another parameter of $K = D/(\Delta U)^n$ is preserved for the 10- and 19-injector combustors. The preserving parameter K is used to match the similar mixing rates of the jets. The motivation for this particular study is that the characteristic time for mixing should be commensurate with the

period of oscillation to drive an instability. This concept is consistent with the Crocco time-lag theory [2,4,5,7,8]. Thus, in order for the two injector configurations to produce the same stability behavior in a chamber with the same resonant frequency, the mixing time should be the same for both configurations. A simple concept is that the mixing time is an eddy turnover time, which is proportional to $D/(\Delta U)^n$. The mixing time increases with an increasing injector diameter D and a decreasing difference between the fuel and oxidizer injection velocities. After several trials, we found the 10- and 19-injector combustors displayed similar instabilities when $n = 1.25$. Table 2 presents the simulation results. Figure 27 shows the pressure history on the combustion-chamber wall at 1.0 cm downstream from the injection plate for cases 10D and 19A. When the injector size is designed by considering the mixing rate effect, the spontaneous longitudinal instability with a similar oscillation frequency can be obtained in the 10- and 19-injector combustors. Another oxygen–fuel mixture ratio of 4:1.1 (i.e., fuel-rich combustion case) is also tested to confirm the
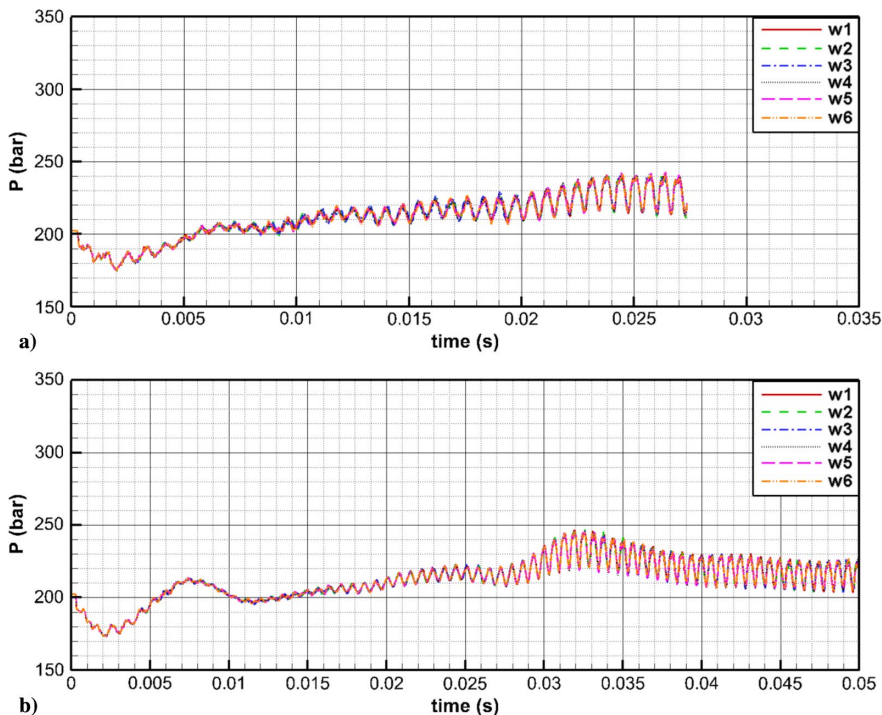

Fig. 27 Pressure histories on the combustion-chamber wall: a) 10D; and b) 19A.
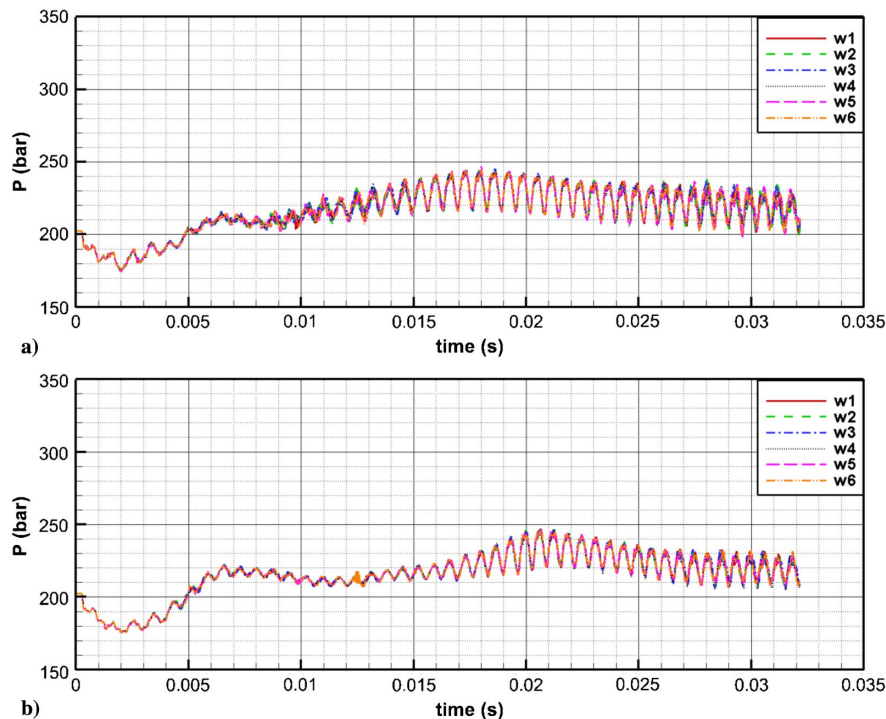
Fig. 28   Pressure histories on the combustion-chamber wall: a) 10E; and b) 19C.

finding. Figure 28 shows the pressure history on the combustion chamber wall at 1.0 cm downstream from the injection plate for cases 10E and 19C with an oxygen–fuel mixture ratio of 4:1.1. The pressure oscillation behaviors for the two cases 10E and 19C are also similar.

IV.   Conclusions

A computational study of the nonlinear combustion instability of a multi-injector rocket engine is presented. Spontaneous and triggered longitudinal instability modes can be observed for the 28-cm-diameter combustion chamber. For the larger-diameter 43 cm combustion chamber, different solutions are obtained with different inlet mass-flux pulsations. A longitudinal instability occurs for the cases without propellant flow pulsation and with moderate $\epsilon = 0.25$ magnitude inlet mass-flux pulsation. The tangential instability is triggered when the magnitude of the inlet mass-flux pulsation is greater than the threshold value of $\epsilon = 0.50$. A pulsed disturbance is able to transfer the oscillation from one unstable mode to another unstable mode.

The large-amplitude tangential pressure wave oscillation enhances the mixing by generation of the streamwise vorticity and the fuel burning efficiency, which results in the higher time-averaged temperature and pressure inside the combustion chamber. The instability generally enhances the mixing and combustion processes: especially in regions of large amplitude. Of course, the enhancement drives the instability wave where the pressure and heat release rate are in phase.

For the 28-cm-diam combustion chamber, a similar combustion instability with 10- and 19-injector geometries is obtained by preserving the mixing rate parameter of $K = D/(\Delta U)^{1.25}$.

Acknowledgments

References

[1] Poinsot, T., and Veynante, D., *Theoretical and Numerical Combustion*, 3rd ed., Aquaprint, Bordeaux, France, 2011, pp. 391–393.

[2] Harrje, D., and Reardon, F., "Liquid Propellant Rocket Combustion Instability," NASA SP 194, 1972.

[3] Oefelein, J. C., and Yang, V., "Comprehensive Review of Liquid-Propellant Combustion Instability in F-1 Engines," *Journal of Propulsion and Power*, Vol. 9, No. 5, 1993, pp. 657–677.
https://doi.org/10.2514/3.23674

[4] Crocco, L., and Cheng, S. L., "High Frequency Combustion Instability in Rockets with Distributed Combustion," *4th International Symposium on Combustion*, Vol. 4, The Combustion Inst., 1953, pp. 865–880.

[5] Crocco, L., and Cheng, S. L., "Theory of Combustion Instability in Liquid Propellant Rocket Motors," AGARD Monograph 8, Neuilly-Sur-Seine, France, 1956.

[6] Sirignano, W. A., and Crocco, L., "A Shock Wave Model of Unstable Rocket Combustors," *AIAA Journal*, Vol. 2, No. 7, 1964, pp. 1285–1296.
https://doi.org/10.2514/3.2534

[7] Mitchell, C. E., Crocco, L., and Sirignano, W. A., "Nonlinear Longitudinal Instability in Rocket Motors with Concentrated Combustion," *Combustion Science and Technology*, Vol. 1, No. 1, 1969, pp. 35–64.
https://doi.org/10.1080/00102206908952190

[8] Zinn, B. T., "A Theoretical Study of Nonlinear Combustion Instability in Liquid-Propellant Rocket Engines," *AIAA Journal*, Vol. 6, No. 10, 1968, pp. 1966–1972.
https://doi.org/10.2514/3.4908

[9] Culick, F. E. C., "Unsteady Motions in Combustion Chambers for Propulsion System," AGARDograph AG-AVT-039, Neuilly-Sur-Seine, France, 2006.

[10] Nguyen, T. M., and Sirignano, W. A., "The Impacts of Three Flamelet Burning Regimes in Nonlinear Combustion Dynamics," *Combustion and Flame*, Vol. 195, No. 10, 2018, pp. 170–182.
https://doi.org/10.1016/j.combustflame.2018.03.031

[11] Miller, K., Sisco, J., Nugent, N., and Anderson, W., "Experimental Study of Combustion Instabilities in a Single-Element Coaxial Swirl Injector," AIAA Paper 2005-4298, 2005.

[12] Sisco, J., Yu, Y., Sankaran, V., and Anderson, W., "Examination of Mode Shapes in an Unstable Model Rocket Combustor," *Journal of Sound and Vibration*, Vol. 330, No. 1, 2011, pp. 61–74.
https://doi.org/10.1016/j.jsv.2010.07.016

[13] Oefelein, J. C., and Yang, V., "Modeling High-Pressure Mixing and Combustion Processes in Liquid Rocket Engines," *Journal of Propulsion and Power*, Vol. 14, No. 5, 1998, pp. 843–857.
https://doi.org/10.2514/2.5349

[14] Nguyen, T. M., Popov, P. P., and Sirignano, W. A., "Longitudinal Combustion Instability in a Rocket Engine with a Single Coaxial Injector," *Journal of Propulsion and Power*, Vol. 34, No. 2, 2018, pp. 354–373.
https://doi.org/10.2514/1.B36516

[15] Urbano, A., Selle, L., Staffelbach, G., Cuenot, B., Schmitt, T., Ducruix, S., and Candel, S., "Exploration of Combustion Instability Triggering Using Large Eddy Simulation of a Multiple Injector Liquid Rocket Engine," *Combustion and Flame*, Vol. 169, July 2016, pp. 129–140.
https://doi.org/10.1016/j.combustflame.2016.03.020

[16] Popov, P. P., Sideris, A., and Sirignano, W. A., "Stochastic Modelling of Transverse Wave Instability in a Liquid-Propellant Rocket Engine," *Journal of Fluid Mechanics*, Vol. 745, April 2014, pp. 62–91.
https://doi.org/10.1017/jfm.2014.96

[17] Sirignano, W. A., and Popov, P. P., "Two-Dimensional Model for Liquid-Rocket Transverse Combustion Instability," *AIAA Journal*, Vol. 54, No. 1, 2013, pp. 1–15.

[18] Popov, P. P., and Sirignano, W. A., "Transverse Combustion Instability in a Rectangular Rocket Motor," *Journal of Propulsion and Power*, Vol. 32, No. 3, 2016, pp. 620–627.
https://doi.org/10.2514/1.B35868

[19] Popov, P. P., Sideris, A., and Sirignano, W. A., "Triggering and Restabilization of Combustion Instability with Rocket Motor Acceleration," *AIAA Journal*, Vol. 54, No. 5, 2016, pp. 1652–1659.
https://doi.org/10.2514/1.J054542

[20] Sirignano, W. A., and Krieg, J., "Coaxial Jet Flame Subject to Long-Wavelength Acoustic Oscillations," *Journal of Propulsion and Power*, Vol. 32, No. 3, 2016, pp. 743–754.
https://doi.org/10.2514/1.B35953

[21] Sirignano, W. A., and Krieg, J., "Two-Time-Variable Perturbation Theory for Liquid-Rocket Combustion Instability," *Journal of Propulsion and Power*, Vol. 32, No. 3, 2016, pp. 755–776.
https://doi.org/10.2514/1.B35954

[22] Nguyen, T. M., Popov, P. P., and Sirignano, W. A., "Driving Mechanisms of Liquid-Propellant Rocket Longitudinal Combustion Instability," *55th AIAA Aerospace Sciences Meeting*, AIAA Paper 2017-0822, 2017.

[23] Menter, F., "Two-Equation Eddy-Viscosity Turbulence Models for Engineering Applications," *AIAA Journal*, Vol. 32, No. 8, 1994, pp. 1598–1605.
https://doi.org/10.2514/3.12149

[24] Strelets, M., "Detached Eddy Simulation of Massively Separated Flows," *39th AIAA Aerospace Sciences Meeting*, AIAA Paper 2001-0879, 2001.

[25] Harvazinski, M., Huang, C., Sankaran, V., Feldman, T., Anderson, W., Merkle, C., and Talley, D., "Coupling Between Hydrodynamics, Acoustics, and Heat Release in a Self-Excited Unstable Combustor," *Physics of Fluids*, Vol. 27, No. 4, 2015, Paper 045102.
https://doi.org/10.1063/1.4916673

[26] Colcord, B., Sirignano, W. A., and Liu, F., "Flameholding in Converging and Turning Channels over Cavities with Periodic Port Injection," *AIAA Journal*, Vol. 51, No. 7, 2013, pp. 1621–1630.
https://doi.org/10.2514/1.J051890

[27] Garby, R., Selle, L., and Poinsot, T., "Large-Eddy Simulation of Combustion Instabilities in a Variable Length Combustor," *Comptes Rendus Mecanique*, Vol. 341, Nos. 1–2, 2013, pp. 220–229.
https://doi.org/10.1016/j.crme.2012.10.020

D. S. Stewart
Associate Editor